

# Measuring the Dark Matter Halo Mass of X-ray AGN at $z \sim 1$ using photometric redshifts

G. Mountrichas<sup>1</sup>, A. Georgakakis<sup>2,1</sup>, A. Finoguenov<sup>3,2</sup>, G. Erfanianfar<sup>2</sup>, M. C. Cooper<sup>4</sup>, A. L. Coil<sup>5</sup>, E. S. Laird<sup>6</sup>, K. Nandra<sup>2</sup>, J. A. Newman<sup>7</sup>

<sup>1</sup>National Observatory of Athens, V. Paulou & I. Metaxa, 11532, Greece

<sup>2</sup>Max Planck Institut für Extraterrestrische Physik, Giessenbachstraße, 85748 Garching, Germany

<sup>3</sup>Department of Physics, University of Helsinki, Gustaf Hallstromin katu 2a, FI-00014 Helsinki, Finlanda

<sup>4</sup>Center for Galaxy Evolution, Department of Physics and Astronomy, University of California, Irvine, 4129 Frederick Reines Hall, Irvine, CA 92697, USA

<sup>5</sup>Department of Physics and Center for Astrophysics and Space Sciences, University of California, San Diego, 9500 Gilman Dr., La Jolla, CA 92093

<sup>6</sup>Astrophysics Group, Blackett Laboratory, Imperial College, Prince Consort Rd, London SW7 2AZ, UK

<sup>7</sup>University of Pittsburgh, Physics & Astronomy Department, 3941 O'Hara Street Pittsburgh, PA, 15260, USA

21 December 2012

## ABSTRACT

Data from the AEGIS, COSMOS and ECDFS surveys are combined to infer the bias and dark matter halo mass of moderate luminosity [ $L_X(2 - 10 \text{ keV}) = 42.9 \text{ erg s}^{-1}$ ] X-ray AGN at  $z \approx 1$  via their cross-correlation function with galaxies. In contrast to standard cross-correlation function estimators, we present a method that requires spectroscopy only for the AGN and uses photometric redshift probability distribution functions for galaxies to determine the projected real-space AGN/galaxy cross-correlation function. The estimated dark matter halo mass of X-ray AGN in the combined AEGIS, COSMOS and ECDFS fields is  $\approx 13h^{-1} M_\odot$ , in agreement with previous studies at similar redshift and luminosity ranges. Removing from the sample the 5 per cent of the AGN associated with X-ray selected groups results in a reduction by about 0.5 dex in the inferred AGN dark matter halo mass. The distribution of AGN in dark matter halo mass is therefore skewed and the bulk of the population lives in moderate mass haloes. This result favour cold gas accretion as the main channel of supermassive black hole growth for most X-ray AGN.

**Key words:** galaxies: active, galaxies: haloes, galaxies: Seyfert, quasars: general, black hole physics

## 1 INTRODUCTION

The clustering properties of Active Galactic Nuclei (AGN) are a powerful diagnostic of the mechanism that dominates the fuelling of Super-Massive Black Holes (SMBHs) across cosmic time. Cold gas accretion scenarios for example, predict that AGN live in Dark Matter Haloes (DMHs) of up to few times  $10^{12} h^{-1} M_\odot$ , almost independent of accretion luminosity and redshift (Marulli et al. 2008; Hopkins et al. 2008). In contrast, if the growth of SMBHs is dominated by accretion from a hot quasi-hydrostatic halo then one might expect more luminous AGN in more massive DMHs (e.g. Fanidakis et al. 2012).

Numerous observational programmes have been initiated in the last few years to test those predictions by measuring the DMH mass of AGN as function of redshift and accretion luminosity. Large spectroscopic campaigns of powerful UV-bright QSOs showed that this population lives in DMHs of a few times  $10^{12} h^{-1} M_\odot$  over a wide range of redshifts (e.g. Croom et al. 2005; da Ângela et al. 2008; Ross et al. 2009). This is consistent with the predictions of cold gas accretion models for the fuelling of the

SMBHs. At the same time there has been progress in the study of the clustering of the less luminous X-ray selected AGN. These systems provide a more representative and less biased census of the active SMBH population that dominates the accretion density of the Universe (e.g. Aird et al. 2010). The DMH masses of this class of sources are estimated to be, on average, larger than those of UV-bright QSOs,  $\log M_{DMH} = 12.5 - 13.5 (h^{-1} M_\odot)$ , Cappelluti et al. 2012). This has been interpreted as evidence against cold-gas accretion via major-mergers in those systems (e.g. Allevato et al. 2011; Mountrichas & Georgakakis 2012). However, there is scatter among the individual measurements of the DMH mass of X-ray AGN, which makes it hard to comment on the redshift and/or accretion luminosity dependence of their clustering properties. This is because both random errors, related to e.g. small sample sizes, and systematic uncertainties, such as sample variance, affect current determinations of the typical DMH mass of X-ray AGN. Both these issues are related to the strong requirement of current clustering estimators for spectroscopy to get robust clustering measurements.

The real-space cross-correlation function of AGN with galax-

ies for example, is arguably one of the most reliable methods for clustering studies (e.g. Coil et al. 2009; Mountrichas & Georgakakis 2012; Krumpe, Miyaji, & Coil 2010; Krumpe, Miyaji, Coil, & Aceves 2012). Random errors are significantly suppressed when counting AGN/galaxy pairs and the impact of sample variance, which is shown to affect even relatively large-area X-ray surveys (e.g. Gilli et al. 2009) is minimised. However, these features do not come for free. The classic method for determining the AGN/galaxy cross-correlation function requires extensive spectroscopy for both AGN and galaxies. This limits the number of X-ray fields that such an analysis can be applied, as spectroscopy for large galaxy samples is expensive in resources. One way to address this limitation is to relax the requirement for spectroscopy in clustering studies.

An important development in the last few years in this direction has been the rapid improvement in the quantity and quality of photometric redshift measurements, particularly for galaxies (e.g. Coupon et al. 2009). Large scale multi-waveband photometric surveys, such as the SDSS (Sloan Digital Sky Survey, Abazajian et al. 2009) and CFHTLS (Coupon et al. 2009), have managed to control random and systematic photometric uncertainties, which in turn translates to large improvements in photometric redshift estimates. This development has motivated methods that use photometric redshifts, in combination with spectroscopy, to determine the clustering of extragalactic populations (Myers et al. 2009; Hickox et al. 2011).

In this paper we present a method similar to that of Myers et al. (2009) that uses photometric redshifts only for galaxies and spectroscopy for X-ray AGN to estimate the AGN/galaxy real-space cross-correlation function and infer the bias and DMH mass of AGN. It is shown that by weighing each galaxy with its photometric redshift Probability Distribution Function yields clustering results similar to those obtained using spectroscopy for both AGN and galaxies. This methodology is then applied to all X-ray fields with public and good quality photometric redshift estimates and extensive spectroscopy for X-ray sources. This translates to a significant increase, compared to previous studies, in the size of the X-ray AGN sample and better control on the impact of sample variance on the results.

In Section 2 the AGN and galaxy samples are presented. The photometric redshift based methodology for the determination of the AGN/galaxy projected real-space cross-correlation function is described in Section 3. The results are presented in Section 4 and are discussed in Section 5. Throughout this paper we adopt  $H_0 = 100 \text{ km s}^{-1} \text{ Mpc}^{-1}$ ,  $\Omega_m = 0.3$  and  $\Omega_\Lambda = 0.7$  and  $\sigma_8 = 0.8$ . Rest frame quantities (e.g. luminosities, dark matter halo masses) are parametrised by  $h = H_0/100$ , unless otherwise stated.

## 2 THE DATA

Three extragalactic survey fields are used to determine the clustering of X-ray AGN at  $z \approx 1$ . The Extended Chandra Deep Field South Survey (ECDFS), the All Wavelength Extended Groth strip International Survey (AEGIS, Davis et al. 2007) and the Cosmological evolution Survey (COSMOS, Scoville et al. 2007). The choice of fields is motivated by the availability of (i) X-ray data, (ii) extensive follow-up spectroscopic programs targeting specifically X-ray sources and (iii) deep multiwavelength imaging (UV, optical, infrared) for the determination of photometric redshift Probability Distribution Functions (PDFs) for individual galaxies.

### 2.1 Optically selected galaxy sample

The COSMOS and AEGIS fields overlap with the D2 and D3 regions respectively, of the deep synoptic Canada-France-Hawaii Telescope Legacy Survey (CFHTLS). The optical photometry (*ugriz* bands) of the T0004 data release is used, which includes photometric redshift estimates reliable to  $i_{AB} < 24 \text{ mag}$  and photometric redshift PDFs (Coupon et al. 2009). Regions of unreliable photometry (CFHTLS catalogue parameter  $\text{FLAG\_TERAPIX} > 1$ ) because e.g. of contamination by bright stars, are masked out. In the analysis we only use CFHTLS optical sources classified as galaxies (CFHTLS parameters  $\text{OBJECT}$  and  $\text{FLAG\_TERAPIX}$  equal to zero), with reliable photometric redshift estimates (CFHTLS parameter  $\text{ZP\_RELIABLE} \neq -99$ ) and  $17.5 < i_{AB} < 24 \text{ mag}$ . Table 1 lists the total number of galaxies used in the D2 and D3 CFHTLS regions.

In the ECDFS the photometric catalogue compiled by the MUSYC collaboration is used (Cardamone et al. 2010). They combined Subaru narrow-band imaging with existing *UBVRIZJHK* photometry and *Spitzer* IRAC images to create a uniform catalogue of  $\sim 40,000$  galaxies to  $R_{AB} = 25.3$ . Reliable photometric redshifts, including PDFs, are also estimated to that magnitude limit (Cardamone et al. 2010). Our analysis uses MUSYC optical sources classified as galaxies (MUSYC catalogue parameter  $\text{STAR\_FLAG} < 1$ ; Cardamone et al. 2010) and magnitudes in the range  $17.5 < i_{AB} < 24 \text{ mag}$ , as for CFHTLS galaxies. Table 1 lists the total number of galaxies used in the MUSYC field.

### 2.2 AGN samples

X-ray AGN are selected from the AEGIS-800 ks survey (AEGIS-XD, Nandra et al. in prep), the Chandra COSMOS survey (C-COSMOS, Elvis et al. 2009) and the ECDFS (Lehmer et al. 2005). The AEGIS-XD covers a total of  $0.3 \text{ deg}^2$  in the Extended Groth Strip to a total depth of 800 ks by combining Chandra ACIS-I observations carried out in AO-3, AO-6 and AO-9. The AEGIS-XD and the ECDFS X-ray source catalogues are generated following the methodology of Laird et al. (2009). For C-COSMOS the source catalogue presented by Elvis et al. (2009) is used. In all three surveys we use all X-rays sources independent of the energy band in which they are detected.

The optical identification of the X-ray sources is based on the Likelihood Ratio method (Sutherland & Saunders 1992) as described in Georgakakis et al. (2009). The AEGIS-XD and COSMOS source lists are matched to the T0004 release optical catalogue of the CFHTLS (Coupon et al. 2009). The ECDFS X-ray sources are cross-matched with the MUSYC photometric catalogue (Cardamone et al. 2010).

Optical spectroscopy of X-ray sources in the AEGIS field is primarily from the DEEP2 (Newman et al. 2012) and DEEP3 galaxy redshift surveys (Cooper et al. 2011b, 2012) as well as observations carried out at the MMT using the Hectospec fibre spectrograph (Coil et al. 2009). Spectroscopic redshifts in the ECDFS have been compiled by Cardamone et al. (2010). We also include redshifts from Silverman et al. (2010) and Cooper et al. (2011a). Redshifts in COSMOS are from the public releases of the VI-MOS/zCOSMOS bright project (Lilly et al. 2009) and the Magellan/IMACS observation campaigns (Trump et al. 2009), as well as the compilation of redshifts for X-ray sources presented by Brusa et al. (2010).

In the clustering analysis we use X-ray sources with  $L_X(2 - 10 \text{ keV}) > 10^{41} \text{ erg s}^{-1}$  and redshifts  $0.7 < z < 1.4$ . The rest-frame 2-10 keV X-ray luminosity is estimated assuming a power-

**Table 1.** Galaxy samples. “Full sample” refers to galaxies in the optical catalogues of the MUSYC, CFHTLS-D2 and D3 after filtering out masked regions and applying the magnitude limits discussed in the text. The “re-sampled” galaxy sample is selected to have redshift distribution similar to that of X-ray AGN. The “DEEP2-like” sample applies the photometric criteria adopted by the DEEP2 redshift survey team to select galaxies in the redshift range 0.7–1.4. For details see Section 3.2 and Appendix A.

field	full sample	“re-sampled” galaxies	“DEEP2-like” galaxies
(1)	(2)	(3)	(4)
CFHTLS (D2)	55,367	28,150	21,731
CFHTLS (D3)	58,665	33,389	23,060
MUSYC	22,730	15,169	9,577

**Table 2.** X-ray AGN samples in the COSMOS, AEGIS-XD and ECDFS fields with  $L_X(2–10\text{ keV}) > 10^{41}\text{ erg s}^{-1}$  and redshifts  $0.7 < z < 1.4$ .

field	No. of sources	$\langle z \rangle$	$\langle \log L_X \rangle$ ( $\text{erg s}^{-1}$ )
COSMOS	182	0.97	43.3
AEGIS-XD	158	0.97	42.5
ECDF-S	101	1.02	42.8

law spectral energy distribution with index  $\Gamma = 1.9$ . The vast majority of sources above this luminosity cut are AGN (Georgakakis et al. 2011). X-ray sources in regions that have been masked out because of poor optical photometry (e.g. bright stars) are excluded from the analysis. Table 2 shows for each field the number of X-ray AGN used for clustering measurements, their mean redshift and average X-ray luminosity.

### 3 METHODOLOGY

#### 3.1 AGN/galaxy Cross-Correlation Function

In real-space, the AGN/galaxy cross-correlation function,  $\xi(r)$ , is given by

$$\xi(r) = \frac{DD(r)}{DR(r)} - 1, \quad (1)$$

where  $DD(r)$  and  $DR(r)$  are the AGN/galaxy and AGN/random pairs at separation  $r$ . The random point catalogue should follow the galaxy sample selection function, i.e. magnitude limit, field boundaries, masked regions.

The distance  $r$  can be decomposed into separations along the line of sight,  $\pi$ , and across the line of sight,  $\sigma$ . If  $s_1$  and  $s_2$  are the distances of two objects 1, 2, measured in redshift-space, and  $\theta$  the angular separation between them, then  $\sigma$  and  $\pi$  are defined as

$$\pi = (s_2 - s_1), \text{ along the line-of-sight}, \quad (2)$$

$$\sigma = \frac{(s_2 + s_1)}{2} \theta, \text{ across the line-of-sight}. \quad (3)$$

The correlation function in redshift-space is then estimated as

$$\xi(\sigma, \pi) = \frac{DD(\sigma, \pi)}{DR(\sigma, \pi)} - 1. \quad (4)$$

This simple estimator has the advantage that the random point source catalogue needs to account only for the selection function of galaxies, which is typically a spatial filter. In contrast more advanced clustering estimators, such as that of Landy & Szalay (1993), require the construction of random catalogues for the X-ray

source population as well. This might introduce systematic biases into the calculations because X-ray observations have variable sensitivity across the field of view, which is challenging to quantify accurately.

In the classic approach of estimating the real-space cross-correlation function, spectroscopic redshifts are available for the AGN and galaxy samples. For each AGN/galaxy pair with  $\sigma$ ,  $\pi$  separations determined from their sky positions and redshifts, the  $DD(\sigma, \pi)$  is incremented by one, i.e.  $DD(\sigma, \pi) = DD(\sigma, \pi) + 1$ . This relation can be modified to account for uncertainties in the determination of the redshifts of the galaxy population. In this case it is assumed that the redshifts of galaxies follow continuous probability distribution functions (i.e. photometric redshifts), while those of AGN are known at a high level of accuracy (i.e. spectroscopic redshifts). For a given galaxy the probability  $f_{gal}$  that it lies at separations  $\sigma$ ,  $\pi$  from an AGN can be estimated from its PDF.  $DD(\sigma, \pi)$  is then incremented by  $f_{gal}$ , instead of unity, i.e.  $DD(\sigma, \pi) = DD(\sigma, \pi) + f_{gal}$ . Therefore, a galaxy may contribute with different probabilities,  $f_{gal}$ , to more than one  $(\sigma, \pi)$  bins of an AGN/galaxy pair.  $DR(\sigma, \pi)$  pairs are estimated following the same procedure. Random catalogues are generated by randomising the positions of galaxies taking into account the geometry and masked regions of each optical survey. In this approach every random point has attached to it the photometric redshift PDF of the galaxy from which it was generated. A total of three random catalogues are produced, one per survey field. Each of them has the same size as the real galaxy catalogue from which it was generated.

When the correlation function is measured in redshift-space, the clustering is affected at small scales by the rms velocity dispersion of AGN along the line of sight and by dynamical infall of matter into higher density regions. To first order, only the radial component of  $\xi(\sigma, \pi)$  is affected by redshift-space distortions. We can therefore remove this bias by integrating along the line of sight,  $\pi$ , to calculate the projected cross-correlation function

$$w_p(\sigma) = 2 \int_0^{\pi_{max}} \xi(\sigma, \pi) d\pi. \quad (5)$$

The maximum scale of the integration is a trade-off between underestimating the clustering amplitude, if  $\pi_{max}$  is too small, and low signal-to-noise ratio, if  $\pi_{max}$  is too large. The optimum  $\pi_{max}$  value is determined by measuring the projected AGN/galaxy cross-correlation function in the combined AEGIS, ECDFS and COSMOS fields (see next section for details) for different  $\pi_{max}$  values in the range  $10 - 100 h^{-1}\text{Mpc}$ . Figure 1 shows that the amplitude of the AGN/galaxy cross-correlation function saturates for  $\pi_{max} = 40\text{ Mpc}$ . This is the value we adopt in the analysis.

Assuming that the real-space AGN-galaxy cross-correlation function follows a power-law of the form  $\xi(r) = (r/r_0)^{-\gamma}$ , we estimate the real-space cross-correlation amplitude,  $r_0$ , and the slope,  $\gamma$  from the relation

$$\frac{w_p(\sigma)}{\sigma} = \left(\frac{r_0}{\sigma}\right)^\gamma \frac{\Gamma(\frac{1}{2})\Gamma(\frac{\gamma-1}{2})}{\Gamma(\frac{\gamma}{2})}, \quad (6)$$

where  $\Gamma(x)$  is the Gamma function. The AGN-galaxy cross-clustering strength can then be expressed in terms of the rms fluctuation of the density distribution over a sphere with a comoving radius of  $8 h^{-1}\text{Mpc}$  (e.g. Miyaji et al. 2007)

$$\sigma_{8,AG}^2 = J_2(\gamma) \left(\frac{r_0}{8 h^{-1}\text{Mpc}}\right)^\gamma, \quad (7)$$

where

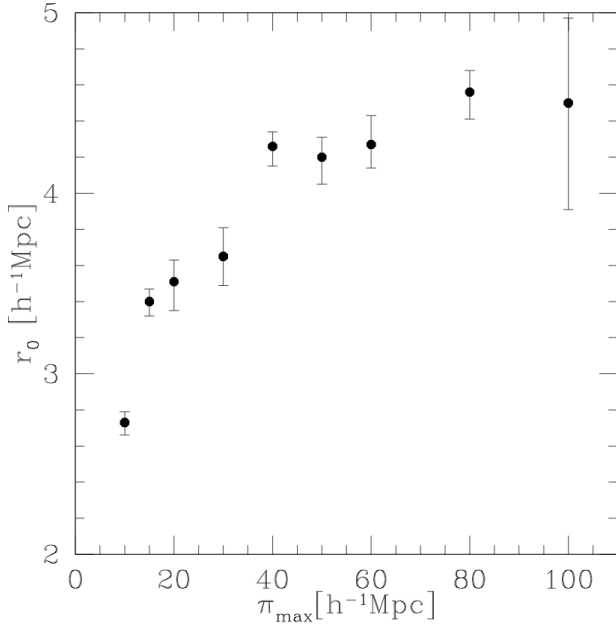


**Figure 1.** The AGN/galaxy cross-correlation length,  $r_0$ , as a function of  $\pi_{\max}$ , the maximum scale of the integration in equation 5. The cross-correlation function is measured by combining the AEGIS, ECDFS and COMSOS fields. The errors are jackknife.

$$J_2(\gamma) = \frac{72}{(3-\gamma)(4-\gamma)(6-\gamma)2^\gamma}, \quad (8)$$

the AGN/galaxy bias,  $b_{AG}$ , can then be calculated via

$$b_{AG} = \frac{\sigma_{8,AG}}{\sigma_8(z)}. \quad (9)$$

### 3.2 Galaxy auto-correlation function and AGN bias

An estimate of the galaxy bias is required to infer the AGN bias from the AGN/galaxy cross-correlation function. If spectroscopy is available for galaxies their bias can be determined from the projected real-space galaxy auto-correlation function (e.g. equations 7 – 9).

In the absence of spectroscopy, the galaxy bias is estimated by deprojecting to 3-D (Limber 1953) their angular auto-correlation function,  $w(\theta)$ . This calculation assumes a power-law form for the correlation function. It also requires knowledge of the redshift distribution,  $N(z)$ , of the galaxy population. The latter is determined by summing the photometric redshift PDFs of galaxies. In section 4.2 we confirm that the galaxy bias inferred from  $w(\theta)$  is consistent with that determined from 3-D clustering analysis using large galaxy spectroscopic surveys like DEEP2.

Care should be exercised in the selection of the galaxy sample for which the bias is estimated to infer the AGN clustering from the cross-correlation function. Fig. 2 shows that the redshift distribution of the overall galaxy population at a given magnitude limit is wide and includes a large fraction of low redshift sources, outside the redshift interval of the X-ray AGN sample (i.e. 0.7–1.4). One expects that the AGN/galaxy cross-correlation signal is dominated by galaxies with photometric redshift PDFs that peak within the redshift interval of the AGN population. It is the bias of those galaxies that should be used to infer the clustering of AGN. Using the full galaxy sample at a given magnitude limit to determine the

AGN bias yields erroneous results. Two approaches are adopted to account for this effect.

The first method limits the galaxy sample by applying appropriate optical colour selection criteria to exclude from the analysis sources outside the redshift range of interest. We adopt the colour selection used by the DEEP2 team to pre-select galaxies in the redshift range 0.7–1.4 (Newman et al. 2012), i.e. at the same redshift range as the X-ray AGN. Appendix A describes how the DEEP2 colour pre-selection is applied to the CFHTLS and MUSYC photometric catalogues. The resulting galaxy samples are referred to as “DEEP2-like”. The total number of galaxies in those samples are listed in Table 1. Figure 2 plots the  $N(z)$  of the “DEEP2-like” galaxy sample in the CFHTLS-D2 field and demonstrates the efficiency of the DEEP2 colour cuts in eliminating sources at  $z < 0.7$ . The size of the “DEEP2-like” galaxy samples in the CFHTLS and MUSYC survey areas is presented in Table 1. This approach has the advantage that one has some control on the properties of the galaxies that go into the cross-correlation function.

The alternative approach is similar to that presented by Hickox et al. (2011). Assume a particular AGN  $i$  at spectroscopic redshift  $z_i$  and a galaxy  $j$  which contributes  $f_{gal,i,j}$  to AGN/galaxy pairs at a particular scale  $DD(\sigma, \pi)$ . For the galaxy  $i$  one can estimate the weight  $w_j = \sum_i f_{gal,i,j}$ , the sum of its contribution to all pairs with all the AGN in the sample at all scales. The quantity  $w_j$  defines the average probability that a particular galaxy participates in the cross-correlation function. One can weigh each galaxy with  $w_j$  to construct the redshift distribution of the galaxies that contribute to the cross-correlation signal. One can then randomly draw samples from the galaxy catalogue that follow the weighted  $N(z)$ . The bias of those galaxies is then used to infer the AGN clustering from the AGN/galaxy cross-correlation function. The galaxy samples produced by this approach are referred to as the “resampling method” samples. Their size in the three survey fields is shown in Table 1. The redshift distribution of the “resampling method” galaxy sample in the CFHTLS-D2 field is presented in Fig. 2.

Equations 7 – 9 are used to measure the AGN/galaxy bias,  $b_{AG}$ , and the galaxy bias,  $b_g$ . The X-ray AGN bias,  $b_{AGN}$ , is

$$b_{AGN} = \frac{b_{AG}^2}{b_g}. \quad (10)$$

The AGN DMH mass is inferred from the bias using the methodology of (e.g. Mo & White 1996). In brief, assuming the ellipsoidal collapse model of Sheth et al. (2001) the bias values are converted to  $\nu = \delta_c/\sigma(M)$  (equation (23) of da Ângela et al. 2008), where  $\sigma(M)$  is the rms fluctuation of the density field and  $\delta_c \approx 1.69$  the critical overdensity required for collapse. Then  $\nu$  is converted to DMH mass using equations (A8)–(A10) of Van den Bosch (2002).

### 3.3 Combining clustering results from different fields

The AGN-galaxy cross-correlation function and galaxy auto-correlation function are determined from the combined AEGIS, COSMOS and ECDFS fields. This is to improve the statistical reliability of the results and minimise the impact of cosmic-variance on the clustering measurements. The combined correlation function is

$$\xi_{all}(r) = \frac{DD_{all}(r)}{DR_{all}(r)} - 1, \quad (11)$$

where

$$DD_{all}(r) = \sum_{i=1}^3 DD_i(r). \quad (12)$$

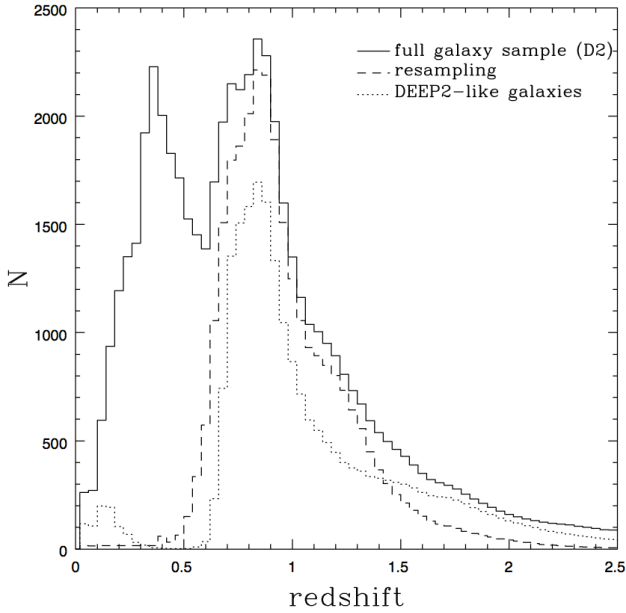


**Figure 2.** Solid line shows the redshift distribution of the full CFHTLS galaxy sample (55,367) in the COSMOS field. Dashed line presents the  $N(z)$  of the “resampling method” galaxy sample (total of 28,150; see Section 3.2). The  $N(z)$  of the “DEEP2-like” galaxies (21,731; see Appendix A) is plotted with the dotted line. The  $N(z)$  of each galaxy population is estimated by summing the photometric redshift PDFs of individual sources.

$DD_i(r)$  is AGN-galaxy pairs in each of the three fields. The same relation is used in the case of DR pairs.

The uncertainties in the correlation function at a given scale are estimated using the Jackknife methodology. Each field is split into five equal-size subregions. This results to a total of 15 sections spread over the three fields of choice. The correlation function is determined 15 times, excluding each time one section. The jackknife error is

$$\sigma^2 = \frac{N-1}{N} \sum_{L=1}^N \frac{DR_L}{DR} [\xi_L - \xi]^2, \quad (13)$$

where  $N$  is the number of sections, i.e. 15,  $DR_L$  is the data-random pairs in each section,  $DR$  is the total number of data-random pairs,  $\xi_L$  is the correlation function measured in each section and  $\xi$  is the combined correlation function. We experimented with different number of Jackknife regions. For a very small number of regions one expects errors dominated by poisson noise. Similarly, for very large number of subregions the sample variance uncertainties become negligible and shot noise is again important. The estimated Jackknife errors normalised to the Poisson errors (excess variance) at a given scale increases initially with the number of Jackknife regions, reaches a plateau and then decreases. The chosen value of 15 Jackknife regions is within the plateau.

## 4 RESULTS

### 4.1 Performance of the photometric redshift based AGN/galaxy cross-correlation method

Before applying the methodology presented in the previous section to the combined AEGIS, ECDFS and COSMOS fields we verify

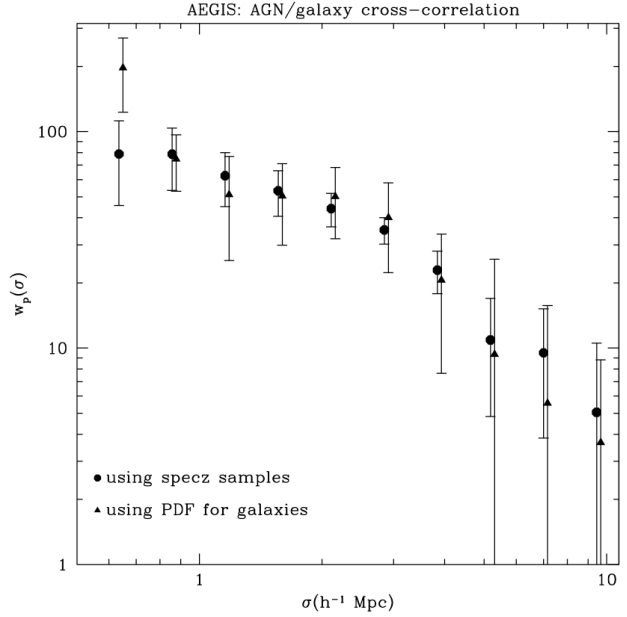


**Figure 3.** The projected real-space AGN/galaxy cross-correlation function in the AEGIS field. Triangles are the cross-correlation function using photometric redshifts only for the galaxy population (CFHTLS-D3). Circles correspond to the cross-correlation function using only galaxies with spectroscopic redshifts from the DEEP2 and DEEP3 surveys. Errors are jackknife. For clarity, triangles are offset in the horizontal direction by  $\delta \log \sigma = +0.01$ .

that it produces similar results with the traditional approach which uses spectroscopic redshift for both the AGN and the galaxy population. In this exercise we use data from the AEGIS field only, which benefits from extensive spectroscopy for galaxies as part of the DEEP2 and DEEP3 surveys (Cooper et al. 2011b, 2012; Newman et al. 2012).

Fig. 3 presents the cross-correlation function of 158 X-ray AGN with  $\sim 5,100$  spectroscopic DEEP2 and DEEP3 galaxies with  $R < 24.1$  mag. This is compared with the projected cross-correlation function estimated by replacing the spectroscopic galaxy sample with  $\sim 23,000$  photometric CFHTLS-D3 “DEEP2-like” galaxies. The estimated AGN bias is  $b_A = 1.93^{+0.40}_{-0.37}$  and  $b_A = 2.05^{+0.21}_{-0.20}$ , for the photo- $z$  based and the standard method, respectively (power law fits are applied on scales  $1-10h^{-1}$  Mpc). The two methods yield consistent results on the inferred bias of AGN.

### 4.2 Determining the bias and DMH mass of X-ray AGN at $z=1$

Fig. 4 presents the projected AGN-galaxy cross-correlation function from the combined AEGIS, ECDFS and COSMOS fields. Two sets of points are plotted. One corresponds to the cross-correlation function with all galaxies and the other to the cross-correlation with the “DEEP2-like” galaxy samples. The two cross-correlation functions are not directly comparable because the galaxy samples used in the calculations are different.

Assuming a power-law form for the cross-correlation function we use a  $\chi^2$  minimization procedure to estimate the best-fit amplitude,  $r_0$ , and the slope,  $\gamma$ , at scales  $1-10h^{-1}$  Mpc, in the linear regime of clustering. The results are shown in Table 3. The fits use only the diagonal elements of the covariance matrix. This does not

affect the best fit values, but may bias the inferred minimum reduced  $\chi^2$  to values lower than unity. The errors correspond to the 68th percentile around the minimum  $\chi^2$ . Non-linearities may affect the correlation function on scales larger than  $1h^{-1}$  Mpc (Ross et al. 2011). Changing our fitting scales to  $0.5 - 10h^{-1}$  Mpc and  $3 - 10h^{-1}$  Mpc, the inferred AGN bias is stable at the 10% level consistent within the errors with the values estimated at scales  $1-10$  Mpc.

Table 3, also presents the AGN-galaxy bias,  $b_{AG}$ , which has been calculated using the best-fit  $r_0$ ,  $\gamma$  and equations 7 – 9. The effective redshift distribution for the cross-correlation function in each of the three fields is estimated by the convolution of the redshift distributions of the AGN and galaxy samples, i.e.  $N_{AG}(z) = N_{AGN}(z) \times N_{gal}(z)$ . The overall redshift distribution is calculated in a similar manner,  $N_{AG}^{all}(z) = N_{AG}^{AEGIS}(z) \times N_{AG}^{COSMOS}(z) \times N_{AG}^{ECDFS}(z)$ .

Figure 5 presents the measurements for the galaxy angular auto-correlation function for the “resampling method” galaxy sample and the “DEEP2-like” galaxies. In fields of finite size the angular auto-correlation function estimation is biased to lower values (integral constraint, Groth & Peebles 1977). The effect of this bias becomes important on scales comparable to the survey size ( $\sim 0.5 - 1$  degrees in our case). Scales in the range  $0.025^\circ \leq \theta \leq 0.2^\circ$  are used to fit the galaxy auto-correlation function. At these scales the integral constraint is negligible. Also, these angular separations correspond to about  $1 - 10 h^{-1}$  Mpc at  $z \approx 1$ , i.e. the scales over which the AGN/galaxy cross-correlation function is measured. Following the procedure described in Section 3.2 the galaxy bias is estimated. The results are listed in Table 3.

As a check, we use spectroscopically confirmed galaxies in the AEGIS-XD field (DEEP2 and DEEP3 surveys) to determine the projected real-space auto-correlation function. This calculation yields  $b_g = 1.78_{-0.11}^{+0.12}$  consistent with the bias of the “DEEP2-like” galaxy sample inferred from the angular auto-correlation function,  $b_g = 1.62 \pm 0.08$  (see Table 3).

Combining the AGN/galaxy projected cross-correlation function with the bias of galaxies inferred from their angular auto-correlation function yields the AGN bias and DMH masses listed in Table 3. The cross-correlation functions using the “resampling method” and the “DEEP2-like” galaxy samples yield  $b_{AGN}$  and DMH masses that are consistent within the statistical uncertainties.

### 4.3 The effect of groups in the clustering signal

In addition to the average dark matter halo mass of AGN, it is also desirable to have information on their distribution in halo mass. Georgakakis et al. (2008) for example found that at  $z \approx 1$  the fraction of X-ray AGN relative to galaxies is similar in groups and in the field, suggesting diverse environments for the AGN population. Recent results on the halo occupation of moderate luminosity X-ray AGN are also consistent with a wide range of halo masses for these sources (Miyaji et al. 2011; Allevato et al. 2012). The signal to noise ratio of our clustering signal is insufficient for halo occupation analysis. We can nevertheless get a handle on the dark matter halos mass distribution of X-ray AGN by investigating how the clustering signal changes once sources in the most massive dark matter haloes within the surveyed area, i.e. groups, are removed.

Groups are identified via their diffuse X-ray emission in the Chandra data of the ECDFS (Finoguenov et al. in prep) and AEGIS-XD (Erfanianfar in prep). In the case of C-COSMOS both the Chandra and the XMM observations (Cappelluti et al. 2009) in that field are used to identify groups (Leauthaud et al. 2010).

The adopted methodology for detecting diffuse X-ray sources is described in Finoguenov et al. (2007) and Leauthaud et al. (2010). Group optical counterparts and redshifts are estimated by searching for red-sequence galaxy overdensities within 0.5 Mpc (physical) off the X-ray centroid. The identification of group members uses the Bayesian approach of George et al. (2011), which estimates the probability that a galaxy belongs to a group given their projected separation, the redshifts of the galaxy and group (including photometric redshift information) and the background density of field galaxies. The groups identified in the COSMOS, AEGIS-XD and ECDFS have masses  $\gtrsim 2 \times 10^{13} M_\odot$  in the redshift range 0.7-1.4. The X-ray group catalogue is by no means complete. It is affected for example, by the variable X-ray sensitivity across the surveyed area, the different depths of the three X-ray fields used in the analysis and scatter in the relation between DMH mass and X-ray luminosity. Nevertheless, using X-ray selected groups allows us to explore, to the first approximation, the impact of the most massive structures within the surveyed area on the AGN clustering signal.

A total of 22 X-ray AGN in the sample (5%, 22/441) are associated with group members, 6 AGN in the ECDFS, 7 in C-COSMOS and 9 in AEGIS-XD. We re-estimate the cross-correlation function after removing this small number of sources from the X-ray AGN catalogue as well as optically selected galaxies within 0.5 Mpc from the X-ray centre of groups. This has a strong impact on the inferred DMH mass. The results are shown in Table 3. A DMH mass of  $12.68_{-0.40}^{+0.27}$  is estimated, about 0.5 dex lower than the full AGN sample. The bulk of the X-ray AGN population at  $z \approx 1$  lives in moderate size dark matter haloes. It should be emphasised that the observed decrease in the clustering signal is related to the way AGN are distributed in halo mass. It is not because of serendipitous massive structures within the surveyed area that bias the inferred DMH mass to high values. The impact of the latter effect on our results is small because of the combination of different fields and the cross-correlation approach we adopt.

### 4.4 Clustering dependence on luminosity

Finally we investigate the dependence of the clustering signal on X-ray luminosity,  $L_X$ . To minimise possible aliases between the redshift and luminosity we first split the AGN sample at the median redshift,  $z = 0.97$ . The X-ray sources in each redshift bin are further separated into two nearly equal size low and high X-ray luminosity subsamples. They are presented in Table 4. Because the number of sources in each subsample is low, we explore differences in the clustering using the relative bias

$$b_{rel} = \sqrt{w_p(\sigma)_{high-L_X} / w_p(\sigma)_{low-L_X}} \quad (14)$$

where  $w_p(\sigma)_{high-L_X}$ ,  $w_p(\sigma)_{low-L_X}$  are the projected cross-correlation functions for the high and low luminosity subsamples, respectively. In this calculation we use scales in the range  $1 - 10h^{-1}$  Mpc. The low- $z$  and high- $z$  subsamples yield  $b_{rel} = 1.25 \pm 0.23$  and  $1.52 \pm 0.35$ , respectively. The uncertainties are too large to comment on the luminosity dependence of the AGN clustering in the present sample.

**Table 3.** Power-law best-fit parameters  $r_0$ ,  $\gamma$  for the AGN/galaxy cross-correlation function and galaxy angular auto-correlation function using the methods discussed in Section 3.2. The  $\chi^2$  fits are using only the diagonal elements of the covariance matrix.  $\chi^2_\nu$  present the reduced  $\chi^2$  values. The inferred biases are also listed. In the case of the cross-correlation function the fit is performed at scales  $1 \leq r \leq 10h^{-1}\text{Mpc}$ . For the galaxy auto-correlation function the fit is on scales  $0.025^\circ \leq \theta \leq 0.2^\circ$ . The inferred AGN bias and DMH mass are also presented.

	$r_0$ ( $h^{-1}\text{Mpc}$ )	$\gamma$	$\chi^2_\nu$ (dof)	$b_{AG}$	$r_0$ ( $h^{-1}\text{Mpc}$ )	$\gamma$	$\chi^2_\nu$ (dof)	$b_g$	$b_{AGN}$	$\log M_{\text{DMH}}$ ( $h^{-1} M_\odot$ )
Resampled galaxies	$5.15^{+0.40}_{-0.44}$	$1.80^{+0.21}_{-0.18}$	0.34 (7)	$1.85^{+0.13}_{-0.14}$	$4.9 \pm 0.3$	$1.70 \pm 0.06$	2.05 (8)	$1.75 \pm 0.08$	$1.96^{+0.29}_{-0.31}$	$12.91^{+0.22}_{-0.31}$
DEEP2-like galaxies	$5.60^{+0.48}_{-0.50}$	$1.72^{+0.25}_{-0.18}$	0.22 (7)	$1.96 \pm 0.15$	$4.5 \pm 0.3$	$1.60 \pm 0.08$	0.96 (8)	$1.62 \pm 0.08$	$2.38 \pm 0.38$	$13.20^{+0.20}_{-0.27}$
AGN in X-ray groups excluded	$4.46^{+0.43}_{-0.46}$	$1.72^{+0.29}_{-0.33}$	0.17 (7)	$1.61^{+0.13}_{-0.14}$	$4.3 \pm 0.3$	$1.55 \pm 0.07$	0.87 (8)	$1.62 \pm 0.08$	$1.71^{+0.29}_{-0.31}$	$12.68^{+0.27}_{-0.40}$

**Table 4.** The number of X-ray AGN in  $z - L_X$  subsamples.

Field	$0.7 < z < 0.97$ $41.0 < L_X < 42.7$	$0.7 < z < 0.97$ $L_X > 42.7$	$0.97 < z < 1.4$ $41.0 < L_X < 43.2$	$0.97 < z < 1.4$ $L_X > 43.2$
COSMOS	25	69	22	66
AEGIS	58	23	56	21
ECDFS	28	17	32	24
Total	111	109	110	111

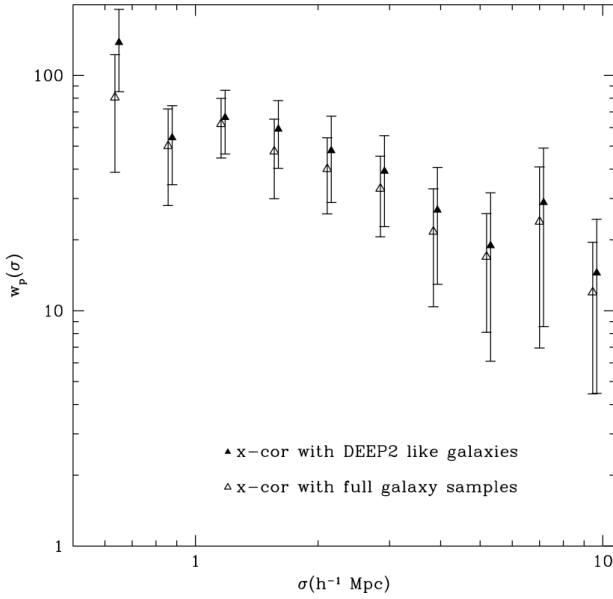


**Figure 4.** AGN-galaxy projected cross-correlation function from the combined AEGIS, COSMOS and ECDFS fields. Filled triangles present the results using the “DEEP2-like” galaxy sample. Open triangles show the results using the full galaxy samples. For clarity, filled triangles are offset in the horizontal direction by  $\delta\log\sigma=+0.01$ .

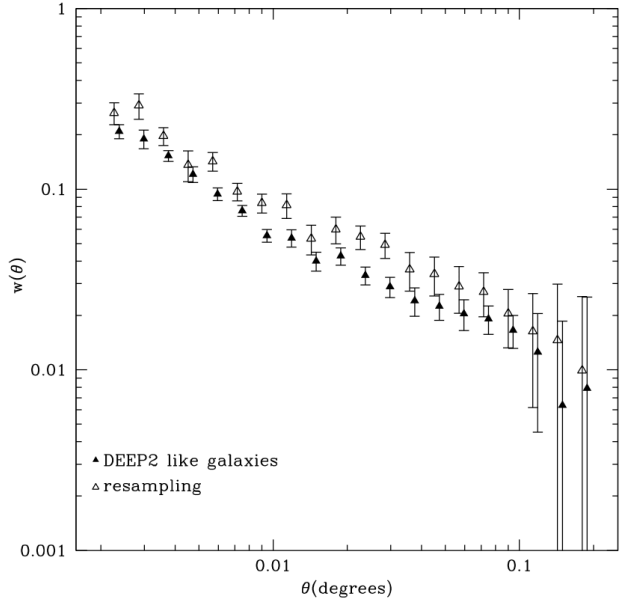


**Figure 5.** Galaxy angular auto-correlation function from the combined AEGIS, COSMOS and ECDFS fields. Filled triangles are the results using the “DEEP2-like” galaxy sample. Open triangles show the results using the “resampling method” galaxy sample. Open triangles are offset by  $-0.02$  in the horizontal axis for clarity.

## 5 DISCUSSION

### 5.1 The clustering estimation method

A method is presented to estimate the projected real-space cross-correlation function between X-ray AGN and galaxies that requires spectroscopy only for the AGN population and uses photometric redshift probability distribution functions for galaxies. The bias of AGN is inferred by estimating the clustering properties of the tracer population, in our case galaxies, from their angular auto-correlation function and (photometric) redshift distribution,  $N(z)$ . A potential

source of systematic error at this step is that the tracer population may have a very different  $N(z)$  from the sources of interest, for which one wishes to estimate the bias. In our case, galaxies have a much wider  $N(z)$ , that includes many low redshift sources, compared to X-ray AGN. Hickox et al. (2011) propose the resampling approach, also used here, to account for this effect. A downside of this methodology is that there is little control on the selection of the galaxies that enter the auto-correlation function determination. These are chosen in a probabilistic manner based on how much they contribute to the cross-correlation clustering signal with AGN.

**Table 5.** Clustering measurements for X-ray AGN from the literature. Columns are: (1) reference to the AGN sample; (2) name of the survey that the AGN sample was selected from; (3) number of sources used; (4) median redshift of the sample; (5) median X-ray luminosity of the sample; (6) the AGN bias values re-calculated using the real-space power law fits quoted in the studies and equations 7 – 9.

Study	Sample	no of objects	$z$	$L_X$ ( $\text{erg s}^{-1}$ )	$b$
(1)	(2)	(3)	(4)	(5)	(6)
This Work (DEEP2-like)	COSMOS/AEGIS-XD/ECDFS	441	0.97	42.9	$2.38 \pm 0.38$
This Work (resampling)	COSMOS/AEGIS-XD/ECDFS	441	0.97	42.9	$1.96^{+0.29}_{-0.31}$
Mountrichas & Georgakakis (2012)	XMM/SDSS	297	0.10	42.1	$1.23^{+0.12}_{-0.17}$
Coil et al. (2009)	AEGIS	113	0.90	43.2	$1.97 \pm 0.25$
Gilli et al. (2005)	CDFN	160	0.96	43.3	$1.87^{+0.14}_{-0.16}$
Gilli et al. (2005)	CDFS	97	0.84	43.5	$2.64 \pm 0.30$
Gilli et al. (2009)	COSMOS	538	0.98	43.4	$3.08^{+0.14}_{-0.16}$
Yang et al. (2006)	CDFN	252	0.8	42.6	$1.77^{+0.20}_{-0.30}$
Yang et al. (2006)	CLASXS	233	1.2	43.8	$3.58^{+0.85}_{-1.11}$
Starikova et al. (2011)	Bootes	1282*	0.37	42.7	$1.55^{+0.15}_{-0.15}$
Starikova et al. (2011)	Bootes	1282*	0.74	43.4	$2.58^{+0.31}_{-0.31}$
Starikova et al. (2011)	Bootes	1282*	1.28	44.0	$2.93^{+0.43}_{-0.43}$
Cappelluti et al. (2010)	BAT	199	0.045	43.5	$1.22^{+0.09}_{-0.08}$
Allevato et al. (2011)	COSMOS	593	1.22		$2.80^{+0.22}_{-0.90}$
Krumpe et al. (2010)	RASS	1552	0.27	43.4	$1.11^{+0.10}_{-0.12}$
Krumpe et al. (2012)	RASS	629	0.13	42.8	$1.19^{+0.08}_{-0.09}$
Krumpe et al. (2012)	RASS	1552	0.25	43.4	$1.06^{+0.09}_{-0.11}$
Krumpe et al. (2012)	RASS	876	0.42	43.8	$0.96^{+0.22}_{-0.54}$

\*This number corresponds to the total number of sources in redshift range  $0.17 < z < 4.5$ .

The resampling approach, and any uncertainties that this may introduce in the results, can be avoided, if the galaxies are selected to have a relatively narrow  $N(z)$  that matches that of X-ray AGN. An example of this approach is the application of the DEEP2 colour cuts to photometrically pre-select galaxies in the redshift interval  $\approx 0.7 - 1.4$ . Resampling is not needed in this case. We demonstrate this point by re-estimating the AGN bias after applying the resampling methodology to the “DEEP2-like” galaxy samples of Table 1. This exercise yields an AGN bias of  $b_A = 2.23^{+0.48}_{-0.50}$ , in good agreement with the bias estimated using the full DEEP2-like samples,  $b_A = 2.38 \pm 0.38$  (see Table 3).

Next we use LRGs (Luminous Red Galaxies) to further demonstrate that a tracer population with a narrow redshift distribution is well suited to the clustering estimation method based on photometric redshifts. Because of their optical SEDs which is dominated by old stars and is characterised by a prominent 4000 Å break, LRGs can be photometrically selected in well defined and relatively thin redshift slices (Eisenstein et al. 2001). We choose to apply our methodology to UV-selected QSOs and LRGs selected in the 2SLAQ (2dF-SDSS LRGs and QSO; Cannon et al. 2006; Ross et al. 2007) survey to estimate the QSO/LRG cross-correlation function and then infer the bias of the QSOs in that survey. We refer the reader to Appendix B for details on the 2SLAQ survey. In short, we use 448 spectroscopically identified UV-bright QSOs and  $\approx 10\,000$  LRGs photometrically selected by 2SLAQ at redshifts  $0.35 - 0.75$ . We associate the  $\approx 10\,000$  2SLAQ LRGs with the photometric redshift PDFs estimated by Cunha et al. (2009) based on the Sloan Digital Sky Survey (SDSS) DR7 photometry. The QSO/LRG real space projected cross-correlation function is estimated using the LRG photometric redshift PDFs. We then estimate the bias of the tracer population using either the full LRG sample or by applying the resampling method of section 3.2. Both approaches give consistent results for the inferred bias of 2SLAQ QSOs,  $b_Q = 1.72^{+0.47}_{-0.44}$  and  $b_Q = 1.58^{+0.50}_{-0.45}$ , respectively (see Ap-

pendix B for details). For tracer populations with relatively narrow redshift distributions there is no need to follow the resampling approach to infer the clustering of the target population (i.e. QSOs).

## 5.2 The clustering properties of X-ray AGN

The AGN/galaxy cross-correlation method of section 3 is applied to the combined AEGIS, COSMOS and ECDFS fields. The inferred bias of X-ray AGN is compared with previous measurements in Figure 6. The literature bias datapoints in that figure are presented in Table 5. They are re-estimated as explained in Mountrichas & Georgakakis (2012). Our bias determinations are consistent with previous studies at similar  $L_X$  and  $z$  intervals that control the impact of sample variance either by combining data from different surveys or by using the AGN/galaxy cross-correlation function. Indeed some the highest bias values of X-ray AGN at  $z \approx 1$  in Figure 6 are because of serendipitous cosmic structures within the surveyed area (e.g. Gilli et al. 2005, 2009).

The picture that emerges from Figure 6 is that moderate luminosity X-ray AGN reside in DMHs with mean mass of about  $10^{13} h^{-1} M_\odot$  from  $z \approx 0$  to  $z = 1$ . However, we also find evidence that this average is skewed to high values as a result of the distribution of AGN in halo mass. Excluding the 5 per cent of the X-ray AGN in the sample associated with X-ray selected groups, reduces the inferred DMH mass of the remaining population by  $\approx 60\%$  to  $\approx 4 \times 10^{12} h^{-1} M_\odot$ . It is emphasised that this is not because of sample variance, in the sense that overdensities within the surveyed area affect the clustering estimation. It is rather a consequence of the way AGN are distributed in DMH mass. Our analysis therefore suggests that a large fraction of the moderate luminosity X-ray AGN at  $z \approx 1$  live in DMHs with masses similar to those of UV bright QSOs, few times  $10^{12} h^{-1} M_\odot$  (e.g. Croom et al. 2005; da Ângela et al. 2008; Ross et al. 2009). This DMH mass scale is consistent with the predictions of models which invoke cold gas



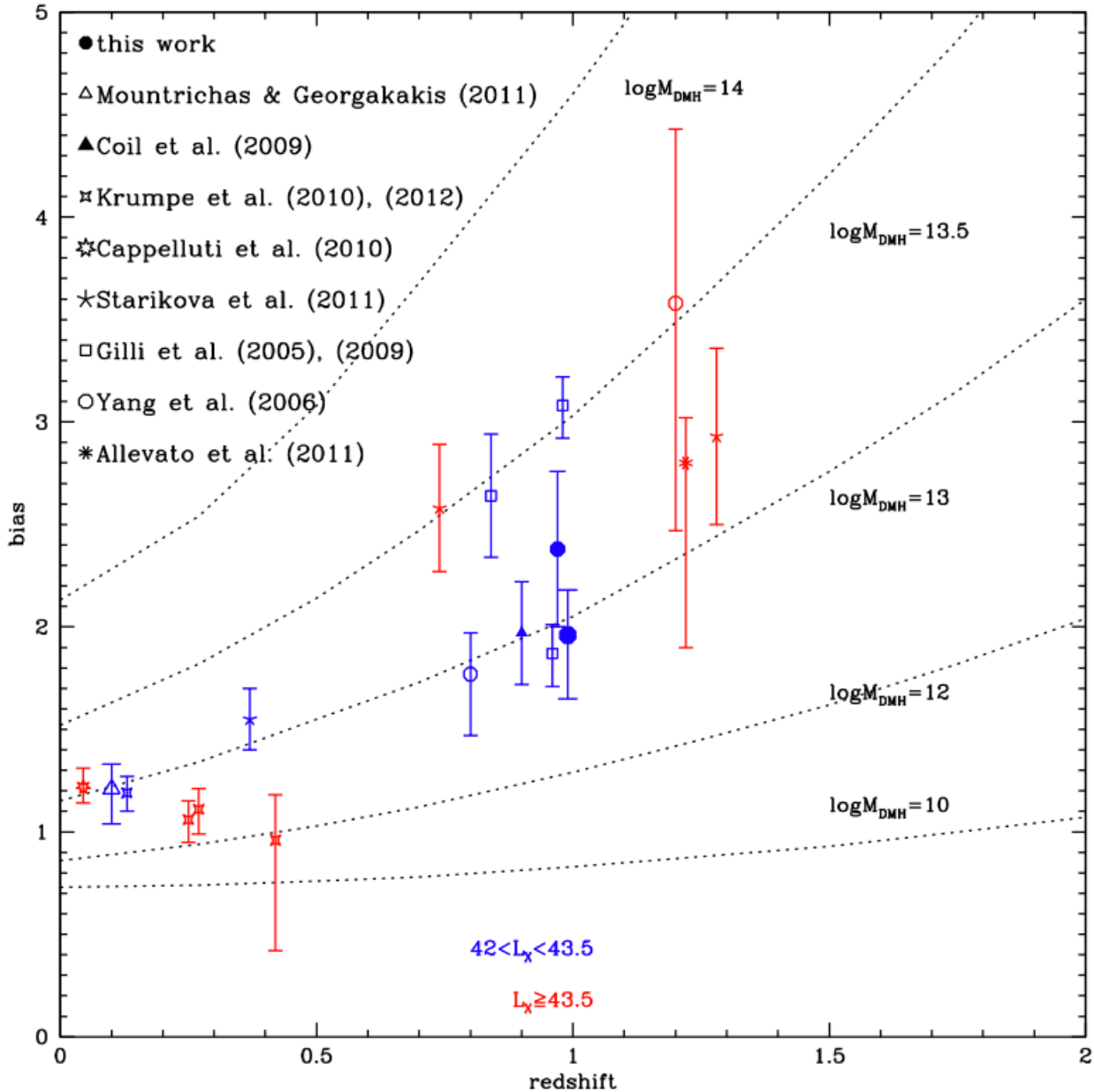


**Figure 6.** The inferred bias of AGN as a function of redshift. Our measurements using both the “DEEP2-like” and the “resampling method” galaxy samples, are plotted with the filled circles. The AGN bias estimation based on the “resampling method” galaxy sample is offset in the horizontal axis by  $\delta z = +0.02$  for clarity. The points have been colour coded based on the median X-ray luminosity of each sample. The dotted lines present the expected  $b(z)$  of DMHs.

accretion via either mergers or disk instabilities to build SMBHs at the centres of galaxies (e.g. Hopkins et al. 2007; Bonoli et al. 2009; Fanidakis et al. 2012). In contrast, if SMBHs grow their mass via accretion of gas from a host quasi-static atmosphere (Croton et al. 2006, e.g.) much larger DMH mass are expected (Fanidakis et al. 2012). Our analysis therefore favours cold gas accretion as the main channel of SMBH growth for X-ray AGN.

## 6 CONCLUSIONS

A method is presented to estimate the bias of any extragalactic population, for which spectroscopy is available, via the estimation of their real space cross-correlation function with a tracer population,

for which only photometric redshift PDFs are available. We argue that this method works best when the tracer population has a narrow redshift distribution that extends over the same range as the sources for which the clustering needs to be estimated.

The method is applied to moderate luminosity [ $L_x(2 - 10 \text{ keV}) \approx 10^{43} \text{ erg s}^{-1}$ ] X-ray AGN at  $z \approx 1$  selected in AEGIS, COSMOS and ECFDS. The tracer population are optically selected galaxies in those fields. DMH masses of  $10^{13} h^{-1} M_\odot$  are estimated for the X-ray AGN samples, in good agreement with previous studies at similar redshift and luminosity intervals.

We also find evidence that the distribution of AGN in dark matter halo mass is skewed. After excluding 5% of the AGN in the sample associated with X-ray groups, we estimate a 0.5 dex lower

DMH mass,  $\log M \approx 12.5$  ( $h^{-1} M_{\odot}$ ). Therefore, the bulk of the X-ray AGN live in environments similar to those predicted by cold gas accretion models for the growth of SMBHs, e.g. gaseous major galaxy mergers or disk instabilities.

## 7 ACKNOWLEDGMENTS

The authors are grateful to the anonymous referee for useful comments and suggestions and Carie Cardamone for providing photometric redshift PDFs for the galaxies in the MUSYC survey field. GM acknowledges financial support from the Marie-Curie Reintegration Grant PERG03-GA-2008-230644. This study makes use of data from AEGIS, a multiwavelength sky survey conducted with the Chandra, GALEX, Hubble, Keck, CFHT, MMT, Subaru, Palomar, Spitzer, VLA, and other telescopes and supported in part by the NSF, NASA, and the STFC. Funding for the DEEP3 Galaxy Redshift Survey has been provided by NSF grants AST-0808133, AST-0807630, and AST-0806732. Based on observations obtained with MegaPrime/MegaCam, a joint project of CFHT and CEA/DAPNIA, at the Canada-France- Hawaii Telescope (CFHT) which is operated by the National Research Council (NRC) of Canada, the Institut National des Sciences de l'Univers of the Centre National de la Recherche Scientifique (CNRS) of France, and the University of Hawaii. This work is based in part on data products produced at TERAPIX and the Canadian Astronomy Data Centre as part of the Canada-France- Hawaii Telescope Legacy Survey, a collaborative project of NRC and CNRS.

## REFERENCES

Abazajian K. N., et al., 2009, *ApJS*, 182, 543  
Aird J., et al., 2010, *MNRAS*, 401, 2531  
Allevato V., et al., 2011, *ApJ*, 736, 99  
—, 2012, *ApJ*, 758, 47  
Arnouts S., Cristiani S., Moscardini L., Matarrese S., Lucchin F., Fontana A., Giallongo E., 1999, *MNRAS*, 310, 540  
Bonoli S., Marulli F., Springel V., White S. D. M., Branchini E., Moscardini L., 2009, *MNRAS*, 396, 423  
Brusa M., et al., 2010, *ApJ*, 716, 348  
Cannon R., et al., 2006, *MNRAS*, 372, 425  
Cappelluti N., Allevato V., Finoguenov A., 2012, *ArXiv e-prints*, 1201.3920  
Cappelluti N., et al., 2009, *A&A*, 497, 635  
Cardamone C. N., et al., 2010, *ApJS*, 189, 270  
Coil A. L., et al., 2004, *ApJ*, 609, 525  
—, 2009, *ApJ*, 701, 1484  
Cooper M. C., et al., 2011a, *ArXiv e-prints*, 1112.0312  
—, 2011b, *ApJS*, 193, 14  
—, 2012, *MNRAS*, 419, 3018  
Coupon J., et al., 2009, *A&A*, 500, 981  
Croom S. M., et al., 2005, *MNRAS*, 356, 415  
Croton D. J., et al., 2006, *MNRAS*, 365, 11  
Cunha C. E., Lima M., Oyaizu H., Frieman J., Lin H., 2009, *MNRAS*, 396, 2379  
da Ângela J., et al., 2008, *MNRAS*, 383, 565  
Davis M., et al., 2007, *ApJ*, 660, L1  
Eisenstein D. J., et al., 2001, *AJ*, 122, 2267  
Elvis M., et al., 2009, *ApJS*, 184, 158  
Fanidakis N., et al., 2012, *MNRAS*, 419, 2797  
Finoguenov A., et al., 2007, *ApJS*, 172, 182

Georgakakis A., Gerke B. F., Nandra K., Laird E. S., Coil A. L., Cooper M. C., Newman J. A., 2008, *MNRAS*, 391, 183  
Georgakakis A., et al., 2009, *MNRAS*, 397, 623  
—, 2011, *MNRAS*, 418, 2590  
George M. R., et al., 2011, *ApJ*, 742, 125  
Gilli R., et al., 2005, *A&A*, 430, 811  
—, 2009, *A&A*, 494, 33  
Groth E. J., Peebles P. J. E., 1977, *ApJ*, 217, 385  
Hickox R. C., et al., 2011, *ApJ*, 731, 117  
Hopkins P. F., Hernquist L., Cox T. J., Keres D., 2008, *ApJS*, 175, 356  
Hopkins P. F., Lidz A., Hernquist L., Coil A. L., Myers A. D., Cox T. J., Spergel D. N., 2007, *ApJ*, 662, 110  
Ilbert O., et al., 2006, *A&A*, 457, 841  
Krumpe M., Miyaji T., Coil A. L., 2010, *ApJ*, 713, 558  
Krumpe M., Miyaji T., Coil A. L., Aceves H., 2012, *ApJ*, 746, 1  
Laird E. S., et al., 2009, *ApJS*, 180, 102  
Landy S. D., Szalay A. S., 1993, *ApJ*, 412, 64  
Leauthaud A., et al., 2010, *ApJ*, 709, 97  
Lehmer B. D., et al., 2005, *ApJS*, 161, 21  
Lilly S. J., et al., 2009, *ApJS*, 184, 218  
Limber D. N., 1953, *ApJ*, 117, 134  
Marulli F., Bonoli S., Branchini E., Moscardini L., Springel V., 2008, *MNRAS*, 385, 1846  
Miyaji T., Krumpe M., Coil A. L., Aceves H., 2011, *ApJ*, 726, 83  
Miyaji T., et al., 2007, *ApJS*, 172, 396  
Mo H. J., White S. D. M., 1996, *MNRAS*, 282, 347  
Mountrichas G., Georgakakis A., 2012, *MNRAS*, 420, 514  
Mountrichas G., Sawangwit U., Shanks T., Croom S. M., P. S. D., Myers A. D., Pimblet K., 2009, *MNRAS*, 394, 2050  
Myers A. D., White M., Ball N. M., 2009, *MNRAS*, 399, 2279  
Newman J. A., et al., 2012, *ArXiv e-prints*, 1203.3192  
Pickles A. J., 1998, *PASP*, 110, 863  
Richards G. T., et al., 2005, *MNRAS*, 360, 839  
Ross A. J., Tojeiro R., Percival W. J., 2011, *MNRAS*, 413, 2078  
Ross N. P., et al., 2007, *MNRAS*, 381, 573  
—, 2009, *ApJ*, 697, 1634  
Scoville N., et al., 2007, *ApJS*, 172, 1  
Sheth R. K., Mo H. J., Tormen G., 2001, *MNRAS*, 323, 1  
Silverman J. D., et al., 2010, *ApJS*, 191, 124  
Sutherland W., Saunders W., 1992, *MNRAS*, 259, 413  
Trump J. R., et al., 2009, *ApJ*, 696, 1195  
Van den Bosch F. C., 2002, *MNRAS*, 331, 98  
First Appendix

## APPENDIX A: COLOUR TRANSFORMATIONS TO THE DEEP2 BRI FILTERSET

The analysis presented in this paper exploits the fact that simple colour cuts provide an efficient way of selecting galaxies in well defined redshift intervals. We choose to study AGN in the redshift range  $0.7 - 1.4$  and therefore adopt the DEEP2 survey photometric criteria for redshift pre-selection (Newman et al. 2012). They showed that galaxies below and above  $z \approx 0.7$  separate well in the  $B - R$  vs  $R - I$  colour space, thereby yielding nearly complete samples of galaxies at  $z > 0.7$ .

Applying the DEEP2 colour cuts to the MUSYC and CFHTLS photometric catalogues requires the determination of transformations between the filtersets of those surveys and the DEEP2 *BRI* photometric bands.

### A1 The MUSYC dataset

In the ECDFS we use the MUSYC Subaru v1.0 catalog which provides photometry in 32 bands from the UV to the mid-infrared (Cardamone et al. 2010). For the DEEP2 we use the photometric catalogue of Coil et al. (2004). As there is no overlap between the MUSYC and any of the DEEP2 fields, the colour transformations between the filtersets in the two photometric surveys are determined using theoretical stellar tracks. The LePHARE code (Arnouts et al. 1999; Ilbert et al. 2006) is used to convolve the DEEP2 and MUSYC  $B$ ,  $R$  and  $I$  filters with the Pickles (1998) stellar templates and predict the  $B - R$  and  $R - I$  colours of stars in the two filtersets. In Figure A1 these stellar tracks are compared with the photometry of optically unresolved sources (i.e. stellar like) in each of the two surveys. In the DEEP2 catalogue these are defined as objects with  $P_{GAL} < 0.2$  (probability that the source is resolved, see Coil et al. 2004 for details) and  $19 < R_{D2} < 23$  mag, where  $R_{D2}$  is the optical magnitude measured in the DEEP2  $R$ -band filter. In the case of the MUSYC catalogue stars are selected by requiring that the parameter `STAR_FLAG` equals unity (see Cardamone et al. 2010 for details) and  $19 < R_M < 23$  mag, where  $R_M$  is the optical magnitude measured in the MUSYC  $R$ -band filter. Figure A1 shows that the photometric calibration of the MUSYC and DEEP2 surveys is offset from the theoretical stellar tracks by about +0.05 and +0.15 mag respectively in the  $R - I$  colour. These systematic offsets should be taken into account when converting from the MUSYC to the DEEP2 filterset. The source of these offsets is beyond the scope of the analysis presented here.

Next we compare the MUSYC and DEEP2 filtersets by plotting in Figure A2 the  $(B - R)_M$  versus the  $(B - R)_{D2}$  and the  $(R - I)_M$  against the  $(R - I)_{D2}$  colours of the Pickles (1998) stellar templates. In the notation above the subscripts M and D2 denote the MUSYC and DEEP2 bands respectively. For simplicity, linear relations are fit to the stellar tracks in Figure A2 to transform the  $(B - R)_M$  and  $(R - I)_M$  colours to  $(B - R)_{D2}$  and  $(R - I)_{D2}$  respectively. Fitting higher order polynomials to the data points in Figure A2 does not change the results. The best-fit linear relations are

$$(B - R)_{D2} = 0.05 + 1.2 (B - R)_M, \quad (\text{A1})$$

$$(R - I)_{D2} = 0.007 + 0.8 (R - I)_M. \quad (\text{A2})$$

Figure A3 plots  $R_M - R_{D2}$  against  $(R - I)_M$  for the Pickles (1998) stellar templates. It shows that  $R_M - R_{D2}$  is well correlated with the  $(R - I)_M$  colour up to  $(R - I)_M \approx 0.5$ . At redder colours the relation appears to flatten and the scatter in the theoretical stellar locus increases. We choose to fit a linear relation to the datapoints up to  $(R - I)_M = 0.5$ . At redder colours, the  $R_M - R_{D2}$  is approximated with a constant fixed to the value of the linear relation at  $(R - I)_M = 0.5$ . Although this approximation may lead to systematic uncertainties in the conversion from  $R_M$  to  $R_{D2}$ , these are expected to be at the level of few tenths of a magnitude. The functional form used to describe the variations of the  $R_M - R_{D2}$  with  $(R - I)_M$  is

$$R_{D2} - R_M = \begin{cases} 0.078 + 0.005 (R - I)_M, & (R - I)_M < 0.5, \\ 0.04, & (R - I)_M > 0.5. \end{cases} \quad (\text{A3})$$

As a consistency check of the colour transformations A1, A2, A3 we compare the magnitude and colour distributions of galaxies in the DEEP2 and MUSYC surveys. For each source in the MUSYC photometric catalogue we estimate its  $(B - R)_{D2}$ ,  $(R - I)_{D2}$  colours and  $R_{D2}$  magnitude by applying the linear relations A1,

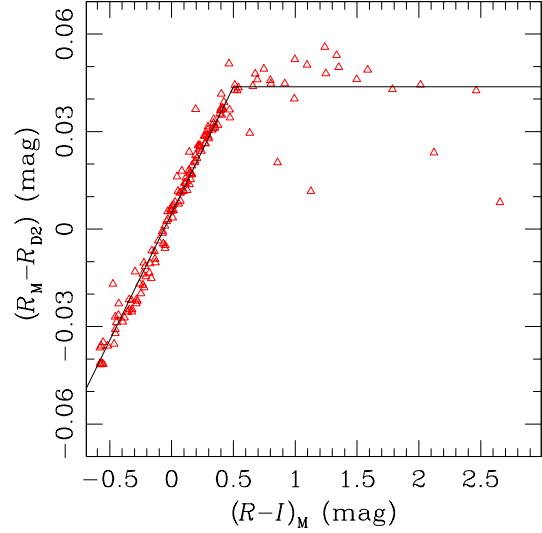


**Figure A3.**  $R_M - R_{D2}$  against  $(R - I)_M$  colour. The red triangles are the Pickles (1998) stellar templates. The black line shows the relation used to approximate the theoretical stellar track.

A2, A3. The number counts in the  $R_{D2}$  band are then constructed for MUSYC sources classified as galaxies (`STAR_FLAG` parameter equals null; see Cardamone et al. 2010 for details). These are then compared with the  $R_{D2}$ -band number counts of DEEP2 galaxies (extended source probability parameter  $P_{GAL} > 0.2$ ; see Coil et al. 2004 for details). The galaxy counts normalised to the area of each photometric survey are plotted in Figure A4. There is a systematic offset of about 0.2 mag between the two photometric catalogues. Similar offsets are also apparent in the  $B_{D2}$  and  $I_{D2}$  galaxy counts. This suggests that the discrepancy is because of differences in the determination of total magnitudes in the two surveys and is not related to the colour transformation between the two filtersets. This is further supported by Figure A5 which compares the  $(B - R)_{D2}$  and  $(R - I)_{D2}$  distributions of the MUSYC and DEEP2 surveys. These are constructed by selecting galaxies in the two surveys with  $18 < R_{D2} < 24$  mag. The faint magnitude limit is chosen to minimise the effect of incompleteness in the shallower DEEP2 photometric survey. In the case of the MUSYC catalogue an offset of +0.2 mag is applied to the estimated  $R_{D2}$  to account for the systematic offset in the number counts of the two surveys. In the case of the  $(R - I)_{D2}$  colour distribution the offsets between the theoretical stellar tracks and the MUSYC/DEEP2 photometry (see Fig. A1) have also been applied to the data. The agreement between the MUSYC and DEEP2 colour distributions in Figure A5 indicates that the colour transformations of equations A1, A2 are robust and can be used to convert the fluxes measured through the MUSYC filterset to the DEEP2  $BRI$  bands.

### A2 The CFHTLS dataset

The CFHTLS D3 field overlaps with the DEEP2 survey in the Extended Groth Strip (EGS). It is therefore possible to determine the transformations from the CFHTLS  $ugriz$  bands to the DEEP2  $BRI$  filterset using sources that are common in the two surveys. The data release T0004 of the CFHTLS photometric catalogue (Coupon et al. 2009) is cross-matched with the DEEP2 source list

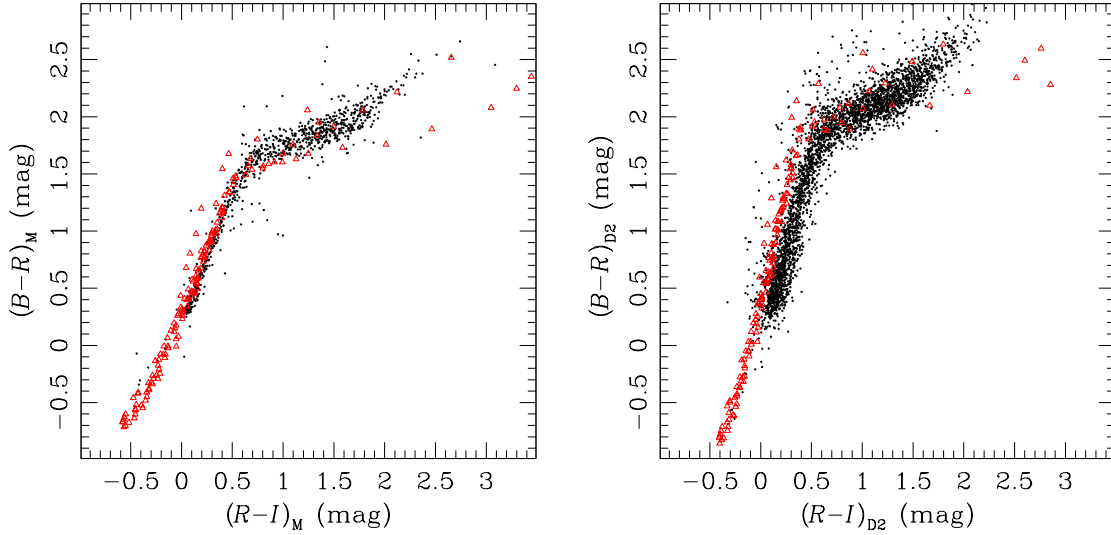


**Figure A1.**  $B - R$  vs  $R - I$  stellar locus. The panel on the left is for the MUSYC filterset (subscript “M” in  $B - R$  and  $R - I$  colours). The right panel is for the DEEP2 bands (subscript “D2”). In both panels the black dots are optically unresolved sources detected in the MUSYC (left) and DEEP2 (right) photometric surveys. The red triangles are the theoretical stellar tracks determined by convolving the Pickles (1998) stellar template library with the MUSYC (left panel) and DEEP2 (right panel)  $BRI$  filters.

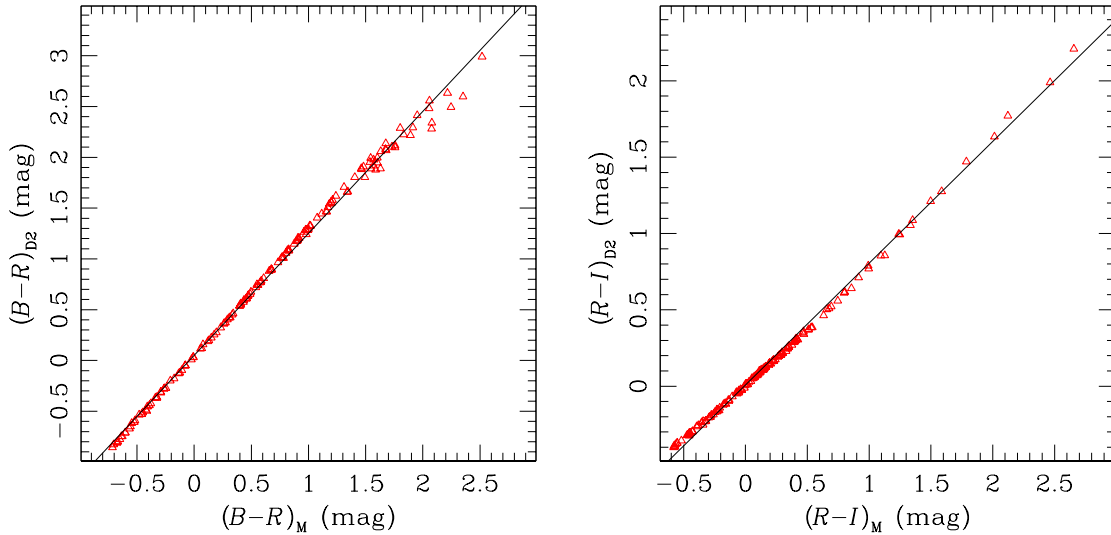


**Figure A2.** **Left panel:**  $(B - R)_{\text{M}}$  colour estimated through the MUSYC bands against  $(B - R)_{\text{D2}}$  colour determined through the DEEP2 filters. The red triangles are the Pickles (1998) stellar templates. The black line shows the best-fit linear relation to the theoretical stellar track. **Right panel:**  $(R - I)_{\text{M}}$  colour estimated through the MUSYC bands against  $(R - I)_{\text{D2}}$  colour determined through the DEEP2 filters. The red triangles are the Pickles (1998) stellar templates. The black line shows the best-fit linear relation to the theoretical stellar track.

(Coil et al. 2004) using a search radius of 2 arcsec. Regions of poor photometry because of nearby bright stars or diffraction spikes are masked out in this exercise.

The transformations of the  $g - r$  and  $r - i$  colours to  $(B - R)_{\text{D2}}$  and  $(R - I)_{\text{D2}}$  respectively are determined using optically resolved sources in the deeper CFHTLS catalogue (parameter FLAG\_TAPIX equals null, Coupon et al. 2009) with  $18 < R_{\text{D2}} < 24$  mag. We choose to use galaxies to determine the transformation between colours in the two filtersets to have a handle on the scatter

expected in those relations because of photometric uncertainties, the different approaches for determining colours in the two surveys as well as the diversity of the Spectral Energy Distributions of extragalactic sources. Figure A6 compares the CFHTLS and DEEP2 filtersets by plotting for galaxies in the overlap region of the two surveys the  $(B - R)_{\text{D2}}$  colour versus  $g - r$  and the  $(R - I)_{\text{D2}}$  colour against  $r - i$ . The mean  $(B - R)_{\text{D2}}$ ,  $[(R - I)_{\text{D2}}]$  and its standard deviation within  $g - r$  ( $r - i$ ) colour bins of 0.1 mag size are also shown in Figure A6. A second order polynomial is fit to

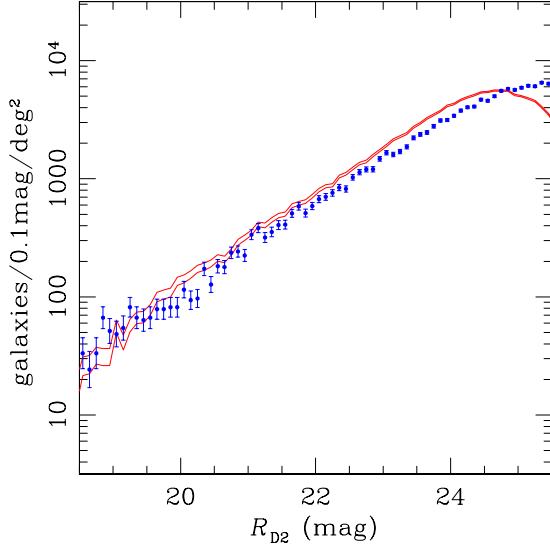


**Figure A4.** Galaxy number counts in 0.1 mag bins for the  $R_{D2}$  filter. The red curves correspond to the 1 sigma rms envelope of the galaxy counts in the DEEP2 photometric survey of the Extended Groth Strip. These observations become incomplete fainter than  $R \approx 24$  mag resulting in the observed turnover at faint magnitudes. The blue dots are for the MUSYC photometric catalogue, in which case  $R_M$  is converted to  $R_{D2}$  using equation A3. The number counts are normalised to the area of each survey,  $0.33 \text{ deg}^2$  in the case of MUSYC and  $1.18 \text{ deg}^2$  for the DEEP2 survey of the Extended Groth Strip. There is systematic offset of about 0.2 mag between the two surveys.

the binned datapoints in the  $(R - I)_{D2}$  versus  $r - i$  plot, while a linear relation is used for the  $(B - R)_{D2}$  against  $g - r$  colour plot.

$$(B - R)_{D2} = 0.04 + 1.63 (g - r), \quad (\text{A4})$$

$$(R - I)_{D2} = 0.054 + 0.84 (r - i) + 0.11 (r - i)^2. \quad (\text{A5})$$

The conversion from the CFHTLS  $r$ -band to the DEEP2  $R_{D2}$  uses optically unresolved sources (i.e. stars). This is because in this case one needs objects with accurate photometry that is least affected by systematics related to e.g. the extent of the source or the determination of aperture corrections. We select optically unresolved sources in the CFHTLS (parameter FLAG\_TAPIX equals unity, Coupon et al. 2009) with DEEP2 counterparts and magnitudes in the range  $18 < R_{D2} < 23$  mag. We choose not to use fainter sources to keep photometric errors small and also to avoid contamination by galaxies at fainter magnitudes. Figure A7 plots  $R_{D2} - r$  against  $r - i$ . Also shown are the average and standard deviation of  $R_{D2} - r$  within  $r - i$  colour bins of 0.2 mag in size. Figure A7 shows the best-fit linear relation to the data

$$R_{D2} - r = -0.01 - 0.19 (r - i), \quad (\text{A6})$$

The  $r$ -band magnitude of each galaxy in the CFHTLS D3 field is converted to  $R_{D2}$  and the corresponding galaxy number counts in that filter are constructed. These are then compared with the galaxy number counts estimated directly from the DEEP2 photometric survey of the EGS field in Figure A8. There is no evidence for systematic offsets in the two distributions.

We also investigate the accuracy of the transformations A4, A5 by comparing the  $(B - R)_{D2}$  and  $(R - I)_{D2}$  distributions of galaxies inferred from the CFHTLS  $gri$  photometry with those estimate directly from the DEEP2 photometric survey in the EGS.

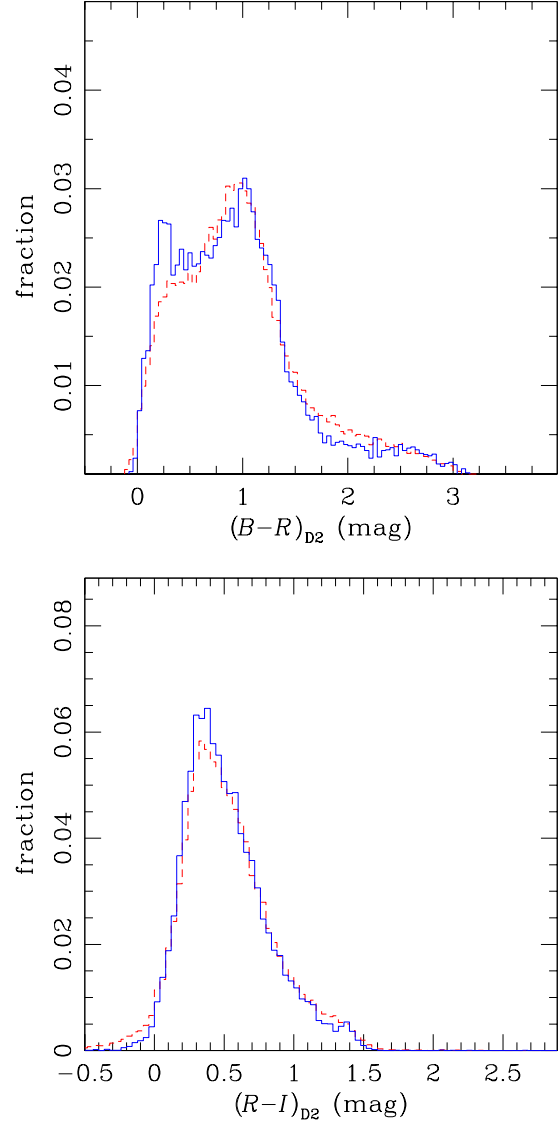


**Figure A5.**  $(B - R)_{D2}$  and  $(R - I)_{D2}$  colour distributions in 0.40 mag bins of galaxies selected in the MUSYC (blue solid line) and DEEP2 (red hatched histogram) surveys. For MUSYC sources the colours are estimated using the colour transformations A1, A2. The colour distribution is limited to galaxies in the two surveys with  $18 < R_{D2} < 24$  mag.

In this exercise we also take into account the scatter of datapoints around the best-fit relations in Figure A6. The rms scatter of the  $(B - R)_{D2}$  versus  $g - r$  relation is estimated to be 0.15 mag. For the  $(R - I)_{D2}$  versus  $r - i$  plot we determine an rms scatter of 0.1 dex. These numbers include photometric errors, differences in the determination of colours in the two surveys as well as any intrinsic scatter in those relations associated with e.g. the diversity of the galaxy SEDs. For each CFHTLS galaxy we apply equations A4, A5 to infer its  $(B - R)_{D2}$  and  $(R - I)_{D2}$ . We then added Gaussian deviates to those colours with Half Width Half Maximum of 0.15 and 0.1 dex respectively. The resulting colour distributions are compared with those determined for galaxies in the DEEP2 photometric survey in Figure A9. This comparison is only for resolved sources in the two surveys with  $18 < R_{D2} < 24$  mag. There is fair agreement between the CFHTLS and DEEP2 colour distributions

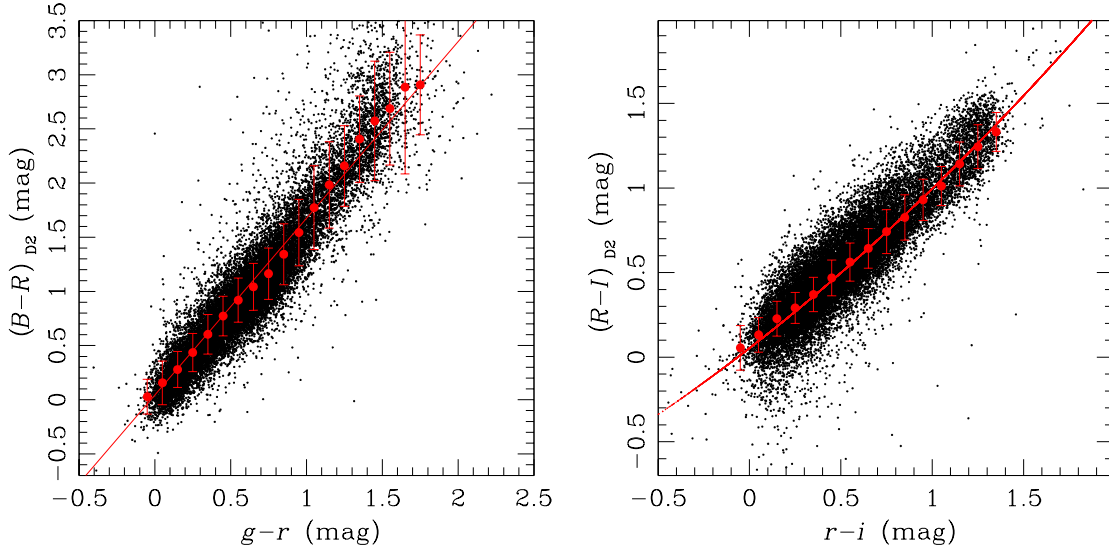


**Figure A6.** **Left:**  $(B - R)_{D2}$  plotted against  $g - r$  colour. The black dots are resolved sources in the D3 region of the CFHTLS (parameter FLAG\_TAPIX equals null, Coupon et al. 2009) with DEEP2 photometric survey counterparts and magnitudes in the range  $18 < R_{D2} < 24$  mag. The mean  $(B - R)_{D2}$  and 1 sigma rms within  $g - r$  bins (0.1 mag size) are shown with the red circles and errorbars. The red line is the best-fit linear relation to those datapoints. The rms scatter around this line is estimated to be about 0.15 mag. **Right:**  $(R - I)_{D2}$  plotted against  $r - i$  colour. The black dots are resolved sources in the D3 region of the CFHTLS with DEEP2 counterparts in the magnitude range  $18 < R_{D2} < 24$  mag. The mean  $(R - I)_{D2}$  and 1 sigma rms within  $r - i$  bins (0.1 mag size) are shown with the red circles and errorbars. The red curve is the best-fit second order polynomial to those datapoints. The rms scatter around this line is estimated to be about 0.1 mag.

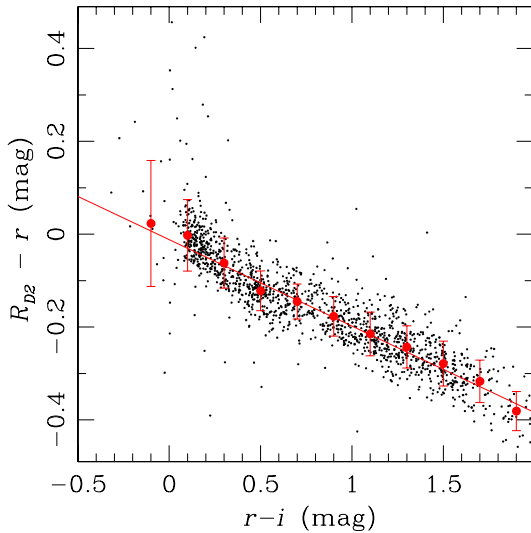


**Figure A7.**  $R_{D2} - r$  plotted against  $r - i$  colour. The black dots are unresolved sources in the D3 region of the CFHTLS (parameter FLAG\_TAPIX equals unity, Coupon et al. 2009) with DEEP2 counterparts in the magnitude range  $18 < R_{D2} < 23$  mag. The mean  $R_{D2} - r$  and 1 sigma rms within  $r - i$  bins (0.2 mag size) are shown with the red circles and errorbars. The red line is the best linear fit to those datapoints.

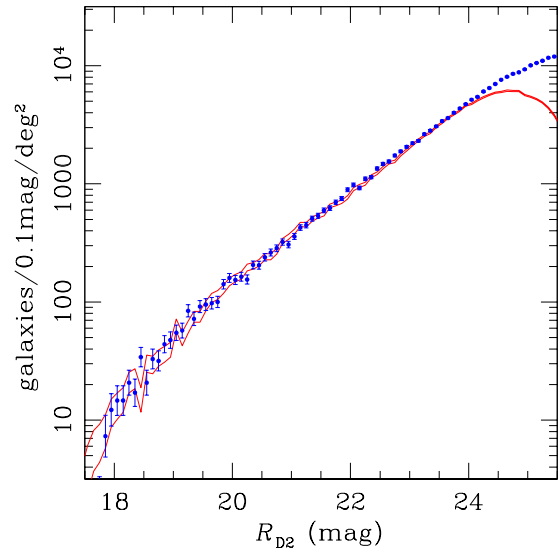


**Figure A8.** Galaxy number counts in  $R_{D2}$  band. The red curves correspond to the 1 sigma rms envelope of the galaxy counts in the DEEP2 photometric survey of the EGS. These observations become incomplete fainter than  $R \approx 24$  mag resulting in the observed turnover at faint magnitudes. The blue dots are the inferred galaxy number counts in the CFHTLS  $r$ -band converted to the  $R_{D2}$  filter using equation A6

suggesting that at least to the first approximation the colour transformations A4, A5 are robust and can be used to convert the fluxes measured through the CFHTLS filterset to the DEEP2  $BRI$  bands.

## APPENDIX B: THE 2SLAQ QSO-LRG SAMPLE

The 2dF-SDSS LRG And QSO survey (Cannon et al. 2006) is a spectroscopic program that used the 2dF facility at the AAT telescope to follow Luminous Red Galaxies in the redshift range 0.35-



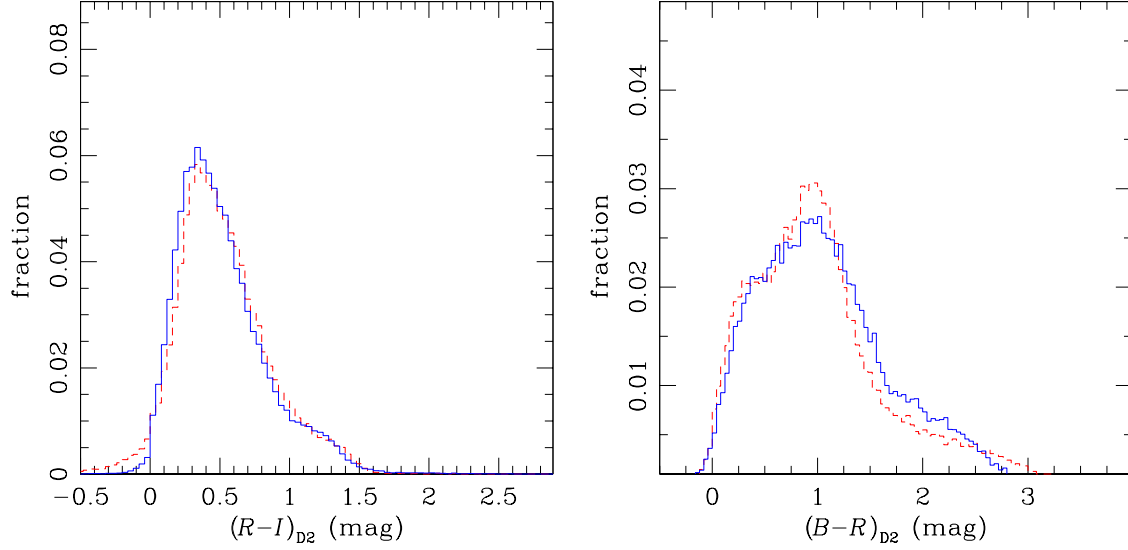


**Figure A9.**  $(B - R)_{D2}$  and  $(R - I)_{D2}$  colour distributions in 0.04 mag bins of galaxies selected in the CFHTLS-D3 (blue solid line) and EGS DEEP2 (red hatched histogram) surveys. For CFHTLS-D3 sources the colours are estimated using the colour transformations A4, A5. The colour distribution is limited to galaxies in the two surveys with  $18 < R_{D2} < 24$  mag.

0.75 and UV-bright QSOs in two equatorial strips covering a total area of  $180 \text{ deg}^2$ . The photometric selection of the LRG and QSO candidates used the SDSS photometry and the colour criteria described by Cannon et al. (2006) and Richards et al. (2005), respectively.

We use data from the northern 2SLAQ strip, which includes 9,923 photometrically selected LRGs and 448 spectroscopically confirmed QSOs in the redshift interval  $z = 0.35 - 0.75$ . The LRG sample is matched to the photometric redshift PDFs determined by Cunha et al. (2009) using the SDSS-DR7 photometry. The QSO/LRG cross-correlation function is then estimated using the methodology described in section 3. The results are plotted in Figure B1. For comparison also shown in that figure is the QSO/LRG cross-correlation signal using spectroscopic for both populations. For this calculation we use the ‘Gold Sample’ of 2SLAQ LRGs (total of 5,500 LRGs Ross et al. 2007), which is the most rigorously defined 2SLAQ LRG sample and has the highest spectroscopic completeness. The fibre collision effect, due to the fact that 2SLAQ QSO had lower priority than 2SLAQ LRGs for spectroscopic observations, is corrected following Mountrichas et al. (2009).

Applying a power law fit, on scales  $1 - 10 h^{-1} \text{ Mpc}$ , and using equations 7–9, the QSO-LRG bias is estimated,  $b_{QL} = 1.92^{+0.17}_{-0.15}$ . The LRG bias is then estimated, using (i) the full photometric LRG sample ( $\approx 10,000$ ) and (ii) the resampling method described in section 3 ( $\approx 6,500$  LRGs). The redshift distributions of the two samples are plotted in Figure B2. The inferred QSO bias is  $b_Q = 1.72^{+0.47}_{-0.44}$  (full sample) and  $b_Q = 1.58^{+0.50}_{-0.45}$  (resampling method). These estimates are consistent within the uncertainties.

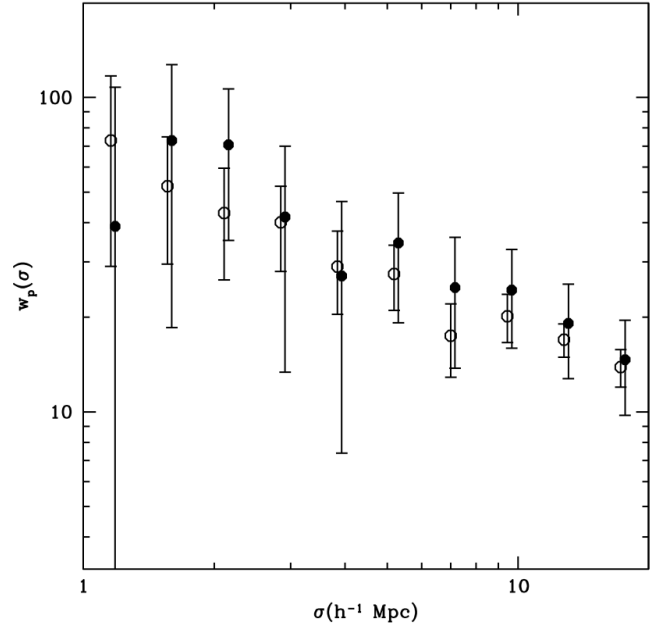


**Figure B1.** QSO/LRG projected real space cross-correlation measurements. Open circles present the results when cross-correlating 448 spectroscopic 2SLAQ QSOs with  $\sim 5,500$  spectroscopic LRGs, in the northern strip of the 2SLAQ survey. Filled circles plot the results when the spectroscopic LRGs have been replaced by  $\sim 10,000$  photometric LRGs. Filled circles have been offset in the horizontal direction by  $\delta \log \sigma = +0.01$  for clarity.

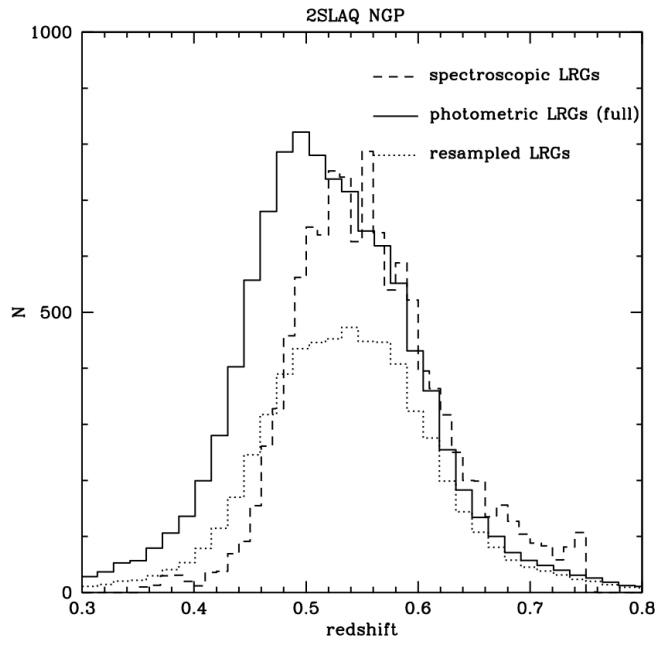


**Figure B2.** The redshift distribution of the 2SLAQ LRG samples used in the analysis.